

NANO EXPRESS

Open Access

Hydrothermal evolution, optical and electrochemical properties of hierarchical porous hematite nanoarchitectures

Wancheng Zhu^{1*}, Xili Cui¹, Xiaofei Liu¹, Liyun Zhang¹, Jia-Qi Huang², Xianglan Piao² and Qiang Zhang^{2*}

Abstract

Hollow or porous hematite (α -Fe₂O₃) nanoarchitectures have emerged as promising crystals in the advanced materials research. In this contribution, hierarchical mesoporous α -Fe₂O₃ nanoarchitectures with a pod-like shape were synthesized via a room-temperature coprecipitation of FeCl₃ and NaOH solutions, followed by a mild hydrothermal treatment (120°C to 210°C, 12.0 h). A formation mechanism based on the hydrothermal evolution was proposed. β -FeOOH fibrils were assembled by the reaction-limited aggregation first, subsequent and *in situ* conversion led to compact pod-like α -Fe₂O₃ nanoarchitectures, and finally high-temperature, long-time hydrothermal treatment caused loose pod-like α -Fe₂O₃ nanoarchitectures via the Ostwald ripening. The as-synthesized α -Fe₂O₃ nanoarchitectures exhibit good absorbance within visible regions and also exhibit an improved performance for Li-ion storage with good rate performance, which can be attributed to the porous nature of Fe₂O₃ nanoarchitectures. This provides a facile, environmentally benign, and low-cost synthesis strategy for α -Fe₂O₃ crystal growth, indicating the as-prepared α -Fe₂O₃ nanoarchitectures as potential advanced functional materials for energy storage, gas sensors, photoelectrochemical water splitting, and water treatment.

Keywords: Hematite, Hierarchical nanoarchitectures, Hydrothermal, Mesoporous, Lithium-ion batteries

Background

Three-dimensional hierarchical architectures, or nanoarchitectures, assembled by one-dimensional (1D) nanostructures have attracted extraordinary attention and intensive interests owing to their unique structures and fantastic properties different from those of the monomorph structures [1-5]. Particularly, hierarchical architectures with mesoporous structures have triggered more and more research enthusiasm in recent years for their high surface-to-volume ratio and permeability. Synthesis of mesoporous materials has become a remarkable level in modern materials chemistry [6]. Mesoporous materials are generally synthesized via a soft- or hard-template-aided process, which usually, however, suffers from the removal of templates and resultant structural collapse, although

hydrothermal synthesis or treatment has been extensively investigated at various stages with the attempt to improve the hydrothermal stability of the as-synthesized mesoporous products. Consequently, great effort has been made to directly grow mesoporous inorganic materials in the absence of any templates in recent years [7,8]. Most recently, the hydrothermal method has emerged as a thriving technique for the facile fabrication of the nanoarchitectures [9-12], such as AlOOH cantaloupe [13], Co(OH)₂ and Co₃O₄ nanocolumns [14], ZnSe nanoflowers [15], Ni(OH)₂ and NiO microspheres [16], and even mesoporous SrCO₃ microspheres [8].

As the most stable iron oxide, hematite (α -Fe₂O₃) has drawn much concern owing to its widespread applications as catalysts, pigments, gas sensors [17], photoelectrodes [17,18], starting materials for the synthesis of magnetic iron oxide nanoparticles (NPs) [19], electrode materials for lithium-ion battery (LIB) [20-26], etc. α -Fe₂O₃ is considered a promising active lithium intercalation host due to its high theoretical capacity (1,007 mAh·g⁻¹), low cost, and environmental friendliness. In

* Correspondence: zhuwancheng@tsinghua.org.cn; zhang-qiang@mails.tsinghua.edu.cn

¹Department of Chemical Engineering, Qufu Normal University, Shandong 273165, China

²Department of Chemical Engineering, Tsinghua University, Beijing 100084, China

contrast to graphite electrodes, the lithium storage within iron oxides is mainly achieved through the reversible conversion reaction between lithium ions and metal nanocrystals dispersed in a Li_2O matrix [24]. Such a process usually causes drastic volume changes ($>200\%$) and severe destruction of the electrode upon electrochemical cycling, especially at a high rate [24]. Particle morphology has been recognized as a key factor influencing the electrochemical performance for lithium storage; thus, hematite nanostructures with different morphologies have been synthesized so as to enhance the electrochemical performance [22]. The mesoporous $\alpha\text{-Fe}_2\text{O}_3$ nanoarchitectures may afford several advantages for LIB application, such as the extended contact area between the active material and the electrolyte as well as the short lithium diffusion length resulting from the thin shell and the hollow space in the central part that buffers the volume expansion during cycling [22,27,28].

Up to now, a family of hierarchical $\alpha\text{-Fe}_2\text{O}_3$ architectures (microring [7], melon-like [25], columnar [29], and nanotube [30] arrays; nanoplatelets [31]; peanut- [32], cantaloupe- [33], or urchin-like [34] nanoarchitectures, etc.) have been available. Most recently, novel hollow architectures (hollow fibers [35], hollow particles [36], hollow microspheres and spindles [37,38], etc.) and porous nanoarchitectures (nanoporous microscale particles [39], mesoporous particles [40,41], nanocrystal clusters [42], porous nanoflowers [43], etc.) have emerged as the new highlights in crystal growth. However, hollow or porous hematite nanoarchitectures were generally fabricated via a forced hydrolysis (100°C , 7 to 14 days) reaction [40], surfactant-assisted solvothermal process [38,42], and hydrothermal- [37] or solvothermal-based [43] or direct [42] calcination (400°C to 800°C) methods. The reported methodologies exhibited drawbacks such as ultralong time or high energy consumption and potentially environmental malignant. It was still a challenge to directly acquire porous/mesoporous hematite nanoarchitectures via a facile, environmentally benign, and low-cost route.

In our previous work, we developed a hydrothermal synthesis of the porous hematite with a pod-like morphology or short-aspect-ratio ellipsoidal shape (denoted as 'pod-like' thereafter) in the presence of H_3BO_3 [44]. However, the process still needed to be optimized, the formation mechanism and the effect of H_3BO_3 were not clear, and properties and potential applications also needed to be further investigated. In this contribution, we report our newly detailed investigation on the optimization of the process and formation mechanism of the mesoporous nanoarchitectures based on the hydrothermal evolution. In addition, the effect of H_3BO_3 was discussed, the optical and electrochemical properties

of the as-synthesized hematite mesoporous nanoarchitectures as well as nanoparticles were investigated in detail, and the application of the as-synthesized mesoporous hematite nanoarchitectures as anode materials for lithium-ion batteries was also evaluated.

Methods

Hydrothermal synthesis of the hierarchical hematite nanoarchitectures

All reagents, such as $\text{FeCl}_3\cdot 6\text{H}_2\text{O}$, NaOH , and H_3BO_3 , were of analytical grade and used as received without further purification. Monodisperse $\alpha\text{-Fe}_2\text{O}_3$ particles were synthesized via a coprecipitation of FeCl_3 and NaOH solutions at room temperature, followed by a facile hydrothermal treatment of the slurry in the presence of H_3BO_3 as the additive. In a typical procedure, 1.281 g of H_3BO_3 was poured into 10.1 mL of deionized (DI) water, then 9.3 mL of FeCl_3 ($1.5\text{ mol}\cdot\text{L}^{-1}$) solution was added, and finally 7.0 mL of NaOH ($4\text{ mol}\cdot\text{L}^{-1}$) solution was dropped into the above mixed solution under vigorous magnetic stirring at room temperature, with the molar ratio of $\text{FeCl}_3/\text{H}_3\text{BO}_3/\text{NaOH}$ as 2:3:4. After 5 min of stirring, 26.4 mL of the resultant brown slurry was transferred into a Teflon-lined stainless steel autoclave with a capacity of 44 mL. The autoclave was sealed and heated to 90°C to 210°C (heating rate $2^\circ\text{C}\cdot\text{min}^{-1}$) and kept under an isothermal condition for 1.0 to 24.0 h, and then cooled down to room temperature naturally. The product was filtered, washed with DI water for three times, and finally dried at 80°C for 24.0 h for further characterization. To evaluate the effects of the molar ratio of the reactants, the molar ratio of $\text{FeCl}_3/\text{H}_3\text{BO}_3/\text{NaOH}$ was altered within the range of 2:(0–3):(2–6), with other conditions unchanged.

Evaluation of the hematite nanoarchitectures as the anode materials for lithium batteries

The electrochemical evaluation of the Fe_2O_3 NPs and nanoarchitectures as anode materials for lithium-ion batteries were carried out using CR2025 coin-type cells with lithium foil as the counter electrode, microporous polyethylene (Celgard 2400, Charlotte, NC, USA) as the separator, and $1.0\text{ mol}\cdot\text{L}^{-1}$ LiPF_6 dissolved in a mixture of ethylene carbonate, dimethyl carbonate, ethylene methyl carbonate (1:1:1, by weight) as the electrolyte. All the assembly processes were conducted in an argon-filled glove box. For preparing working electrodes, a mixed slurry of hematite, carbon black, and polyvinylidene fluoride with a mass ratio of 80:10:10 in *N*-methyl-2-pyrrolidone solvent was pasted on pure Cu foil with a blade and was dried at 100°C for 12 h under vacuum conditions, followed by pressing at $20\text{ kg}\cdot\text{cm}^{-2}$. The galvanostatic discharge/charge measurements were performed at different current densities in the voltage range

of 0.01 to 3.0 V on a Neware battery testing system (Shenzhen, China). The specific capacity was calculated based on the mass of hematite. Cyclic voltammogram measurements were performed on a Solartron Analytical 1470E workstation (Farnborough, UK) at a sweep rate of $0.1 \text{ mV}\cdot\text{s}^{-1}$.

Characterization

The crystal structures of the samples were identified using an X-ray powder diffractometer (XRD; D8-Advance, Bruker, Karlsruhe, Germany) with a $\text{Cu K}\alpha$ radiation ($\lambda = 1.5406 \text{ \AA}$) and a fixed power source (40.0 kV, 40.0 mA). The morphology and microstructure of the samples were examined using a field-emission scanning electron microscope (SEM; JSM 7401 F, JEOL, Akishima-shi, Japan) operated at an accelerating voltage of 3.0 kV. The size distribution of the as-synthesized hierarchical architectures was estimated by directly measuring *ca.* 100 particles from the typical SEM images. The N_2 adsorption-desorption isotherms were measured at 77 K using a chemisorption-physisorption analyzer (Autosorb-1-C, Quantachrome, Boynton Beach, FL, USA) after the samples had been outgassed at 300°C for 60 min. The specific surface area was calculated from the adsorption branches within the relative pressure range of 0.10 to 0.31 using the multipoint Brunauer-Emmett-Teller (BET) method, and the pore size distribution was evaluated from the N_2 desorption isotherm using the Barrett-Joyner-Halenda method. The optical properties were examined using a UV-vis spectrophotometer (Cary 300, Varian, Palo Alto, CA, USA), with absolute alcohol as the dispersive medium.

Results and discussion

Hematite structures obtained at different molar ratios of the reactants

Figure 1 shows the influences of the molar ratio of $\text{FeCl}_3/\text{H}_3\text{BO}_3/\text{NaOH}$ on the compositions and morphologies of the hydrothermal products obtained at 150°C for 12.0 h. When changing the molar ratio of $\text{FeCl}_3/\text{H}_3\text{BO}_3/\text{NaOH}$ within the range of 2:(0–3):(2–6), all products were composed of pure-phase hematite ($\alpha\text{-Fe}_2\text{O}_3$, JCPDS No. 33–0664), with a detectable slight difference of the crystallinity (Figure 1a). With the molar ratio of $\text{FeCl}_3/\text{H}_3\text{BO}_3/\text{NaOH}$ changed from 2:0:6 to 2:0:4 and to 2:0:2, the crystallinity of hematite decreased slightly (Figure 1a₁,a₂,a₃). In contrast, the morphologies of the obtained products varied significantly with the change of the molar ratio of reactants. Quasi-spherical hematite NPs with a diameter of 30 to 150 nm were obtained when the molar ratio of $\text{FeCl}_3/\text{H}_3\text{BO}_3/\text{NaOH}$ was 2:0:6 (Figure 1b,b₁), similar to the so-called $\alpha\text{-Fe}_2\text{O}_3$ nanopolyhedra synthesized in the ammonia-water system at 180°C for 8.0 h [23]. With the molar ratio decreased to 2:0:4 and 2:0:2, hierarchical pod-like (with elliptical ends

and relatively uniform diameter along the long axial direction, Figure 1c) and peanut-type nanoarchitectures (with relatively sharp elliptical ends and saddle-shaped middle part, Figure 1d,d₁) were acquired, respectively. The pod-like architectures contained 1D or linear chain-like assemblies of smaller nanoparticles or rod-like subcrystals within the body (as shown in red dotted elliptical and rectangular regions in Figure 1c), with distinct cavities on the surfaces (Figure 1c). The peanut-type nanoarchitectures (Figure 1d,d₁) also comprised small nanoparticles within the body whereas with not so distinct cavities on the surfaces owing to the relatively compact assembly. Similar 1D assemblies, such as rod-like subcrystals and linear chains of interconnected primary particles, have also been found to exist as the subunits of peanut-type [45] and double-cupola [46] hematite, respectively. Obviously, the molar ratio of 2:0:6 ($\text{FeCl}_3/\text{H}_3\text{BO}_3/\text{NaOH}$) led to nearly monodisperse hematite NPs, whereas the molar ratio of 2:0:4 and 2:0:2 resulted in porous hierarchical architectures with different morphologies. According to Sugimoto's research [45,47,48], size control is generally performed by controlling the number of nuclei during the nucleation stage, and nucleation occurs during the addition of NaOH solution into FeCl_3 solution. In the present case, the molar ratio of $\text{FeCl}_3/\text{H}_3\text{BO}_3/\text{NaOH}$ as 2:0:6 is the stoichiometric ratio for the formation of colloidal $\text{Fe}(\text{OH})_3$ at room temperature, which led to the greatest degree of supersaturation of $\text{Fe}(\text{OH})_3$ and further resulted in the largest number of nuclei and ultimately brought the quasi-spherical $\alpha\text{-Fe}_2\text{O}_3$ NPs.

However, when H_3BO_3 was introduced into the reaction system, e.g., the molar ratio of $\text{FeCl}_3/\text{H}_3\text{BO}_3/\text{NaOH}$ was designed as 2:0.3:4 (Figure 1a₄,e,e₁) and 2:1.5:4 (Figure 1a₅,f,f₁), relatively uniform porous pod-like hematite nanoarchitectures were obtained. For the ratio of 2:0.3:4, 90% of the nanoarchitectures have an aspect ratio (ratio of longitudinal length to latitude diameter) within 1.4 to 1.8 (Figure 1e₁). For the hematite obtained from a molar ratio of $\text{FeCl}_3/\text{H}_3\text{BO}_3/\text{NaOH}$ as 2:1.5:4, 95% of the nanoarchitectures have an aspect ratio within 1.4 to 1.8 (Figure 1f₁). Therefore, the introduction of H_3BO_3 not only preserved the shape of hematite particles, but also improved the morphology uniformity of the nanoarchitectures. This situation was different from that of the formation of peanut-type hematite, which evolved from pseudocubic particles via an ellipsoidal shape with the increasing concentration of the additive such as sulfate or phosphate [49]. On the other hand, compared with those organic surfactant-assisted solvothermal or other solution-based calcination methods, the introduced H_3BO_3 in the present case could be easily removed via DI water washing and then reused, indicating the environmentally benign characteristic.

Effects of hydrothermal temperature on the hematite product formation

The compositions and morphologies of the hydrothermal products obtained at various temperatures for 12.0

h were tracked so as to further understand the corresponding evolution, as shown in Figure 2. Obviously, the hydrothermal temperature had significant influences on the compositions as well as the morphologies of the

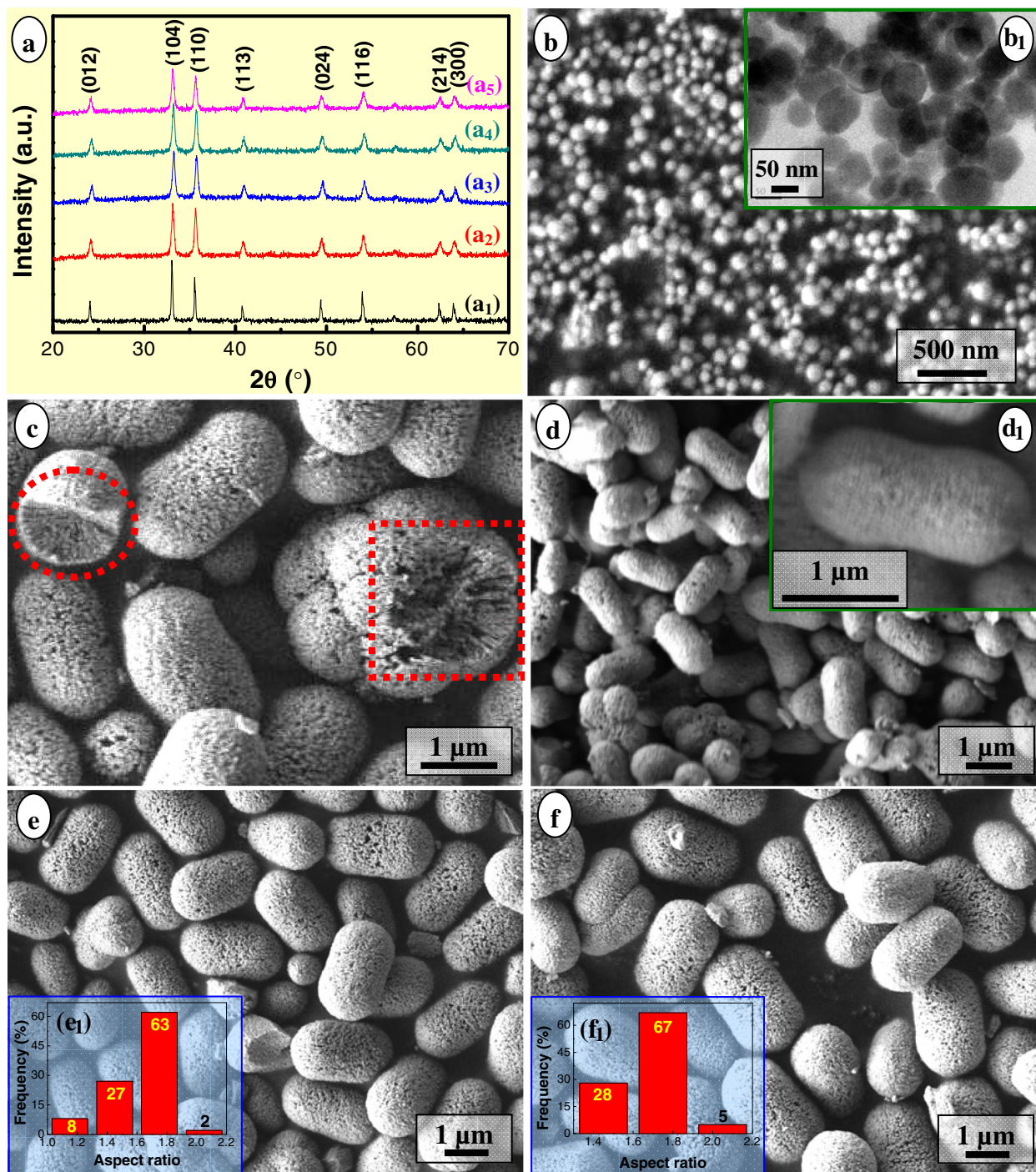


Figure 1 XRD patterns (a) and SEM (b, c-f) and TEM (b₁) images of the hydrothermal products. The products were obtained at 150°C for 12.0 h with different molar ratios of $\text{FeCl}_3/\text{H}_3\text{BO}_3/\text{NaOH} = 2:0:6$ (a₁, b, b₁), $2:0:4$ (a₂, c), $2:0:2$ (a₃, d, d₁), $2:0:3:4$ (a₄, e, e₁), $2:1.5:4$ (a₅, f, f₁). Inset: aspect ratio distributions of the corresponding samples (e₁, f₁).

products. The sample hydrothermally treated at 90°C was composed of relatively poor-crystallinity and low-aspect-ratio akaganeite (β -FeOOH, JCPDS No. 34-1266, Figure 2a₁) nanorods or nanofloccules (Figure 2b). When hydrothermally treated at 105°C, the product gradually changed into poor-crystallinity α -Fe₂O₃ (Figure 2a₂, JCPDS No. 33-0664) of pod-like and pumpkin-like

nanoarchitectures (Figure 2c). Moreover, the local details showed that the nanoarchitecture consisted of short 1D nanostructured subunits and tiny NPs (Figure 2c₁). When treated at 120°C, α -Fe₂O₃ nanoarchitectures with greatly improved crystallinity (Figure 2a₃) and uniform compact pod-like morphology (Figure 2d) were formed, 87% of which had a longitudinal length of 2.2 to 2.5 μ m

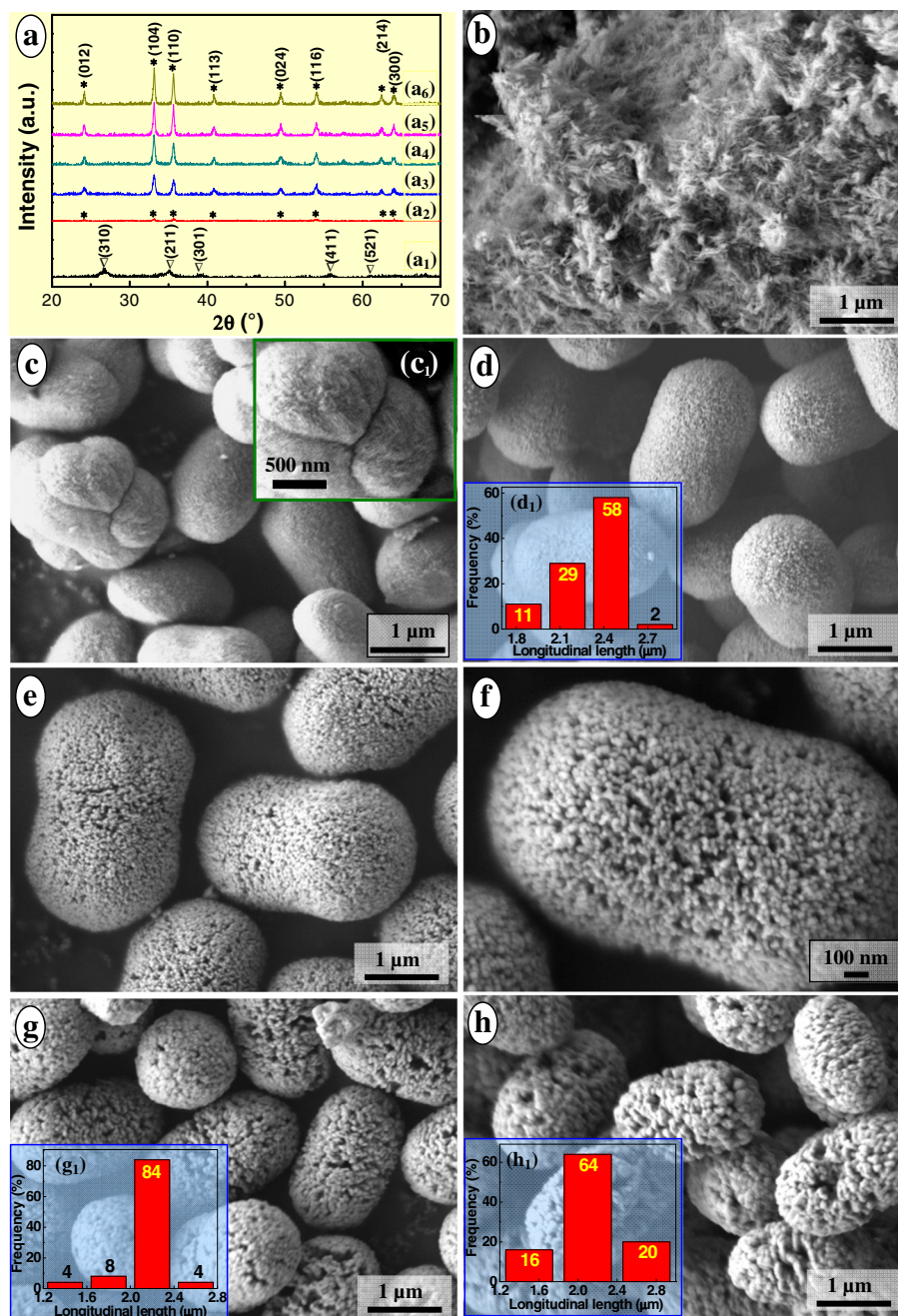


Figure 2 XRD patterns (a) and SEM images (b-h) of the hydrothermal products. The products were synthesized at different temperatures for 12.0 h, with the molar ratio of FeCl₃/H₃BO₃/NaOH = 2:3:4. Temperature (°C) = 90 (a₁, b), 105 (a₂, c), 120 (a₃, d), 150 (a₄, e, f), 180 (a₅, g), 210 (a₆, h). Inset: high-resolution SEM image (c₁) as well as the longitudinal length distributions (d₁, g₁, h₁) of the corresponding samples. The asterisk represents hematite (α -Fe₂O₃, JCPDS No. 33-0664); nabla represents akaganeite (β -FeOOH, JCPDS No. 34-1266).

(Figure 2d₁). Notably, the compact nanoarchitecture contained numerous tiny NPs onto the surfaces. With the temperature increasing up to 150°C and keeping it constant for 12.0 h, the products comprised uniform porous pod-like α -Fe₂O₃ with higher crystallinity (Figure 2a₄) and multitudinal cavities on the surfaces (Figure 2e, f), 84% of which had a longitudinal length of 2.6 to 3.2 μ m [44]. The morphology of the present pod-like α -Fe₂O₃ nanoarchitectures was somewhat similar to that of the melon-like microparticles by the controlled H₂C₂O₄ etching process [25]. With the temperature further going up to 180°C, porous pod-like α -Fe₂O₃ nanoarchitectures with further improved crystallinity (Figure 2a₅) and more and larger cavities on the surfaces were obtained (Figure 2g), 84% of which had a longitudinal length of 2 to 2.4 μ m (Figure 2g₁). When hydrothermally treated at 210°C for 12.0 h, the product evolved into high-crystallinity whereas entirely loose porous α -Fe₂O₃ nanoarchitectures (Figure 2a₆,h), 84% of which had a longitudinal length of 2.1 to 2.7 μ m (Figure 2h₁).

It was worth noting that when treated at a temperature from 90°C to 210°C for 12.0 h, the overall crystallinity of the products became higher (Figure 2a₂, a₃,a₄,a₅,a₆), and the NPs and cavities within the α -Fe₂O₃ nanoarchitectures grew larger. The product evolved from compact pod-like nanoarchitectures (Figure 2c,d)

to loose (Figure 2e,f) and to looser (Figure 2g,h) pod-like nanoarchitectures. As a matter of fact, with the temperature going up from 120°C to 150°C, to 180°C, and to 210°C, the crystallite size along the [104] direction, i.e., D_{104} , calculated by the Debye-Scherrer equation also increased from 23.3 to 27.3, to 28.0, and to 31.3 nm, respectively. This was in accordance with the direct observation on the gradual increase in the NP size within the nanoarchitectures (Figure 2d,e,f,g,h), thus accounted for the gradual sharper tendency for the XRD patterns of the corresponding hydrothermal products (Figure 2a₃,a₄,a₅,a₆) obtained from 120°C to 210°C. Analogous to those obtained previously (Figure 1c,e,f), the nanoarchitectures obtained at 150°C to 210°C for 12.0 h were speculated to be constituted of 1D assemblies (Figure 2e,f) or NPs (Figure 2g,h).

Determination of the mesoporous structure of the pod-like α -Fe₂O₃ nanoarchitectures

Figure 3 shows the N₂ adsorption-desorption isotherms and corresponding pore size distributions of the hydrothermally synthesized α -Fe₂O₃ nanoarchitectures with typical morphologies. Influences of the temperature on the porous α -Fe₂O₃ nanoarchitectures are summarized in Table 1. As listed, the selected nanoarchitectures 1, 2, 3, and 4 corresponded with those obtained at 120°C

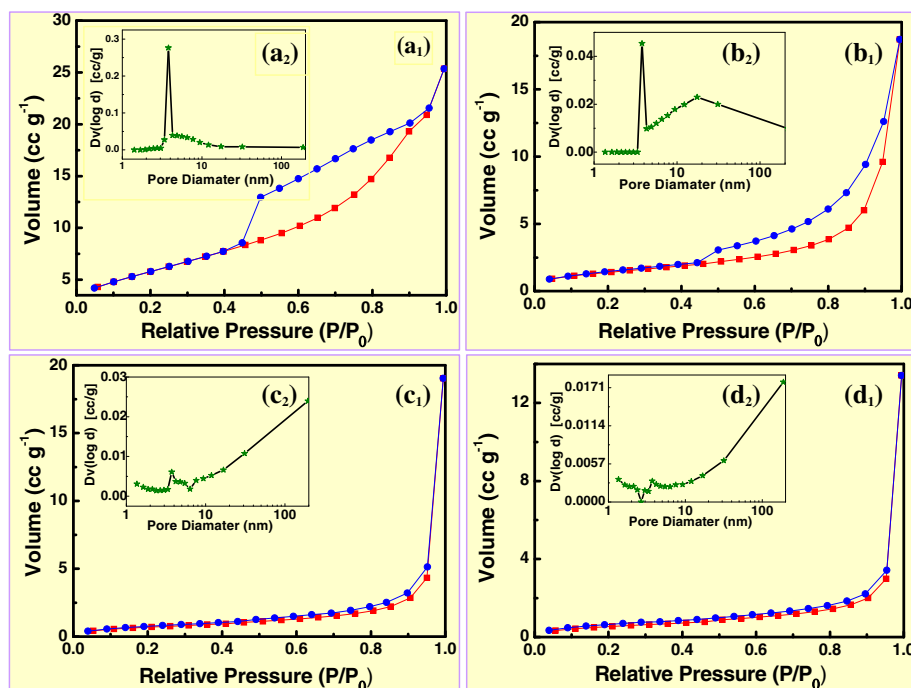


Figure 3 Nitrogen adsorption-desorption isotherms (a₁-d₁) and corresponding pore diameter distributions (a₂-d₂) of the mesoporous α -Fe₂O₃. The nanoarchitectures were synthesized at different temperatures for 12.0 h, with the molar ratio of FeCl₃/H₃BO₃/NaOH = 2:3:4. Temperature (°C) = 120 (a₁, a₂); 150 (b₁, b₂); 180 (c₁, c₂); 210 (d₁, d₂). The blue line with blue circles represents the desorption curve; the red line with square rectangles represents the adsorption curve.

(Figure 2d), 150°C (Figure 2e,f), 180°C (Figure 2g), and 210°C (Figure 2h) for 12.0 h, respectively. All N_2 adsorption-desorption isotherms of the nanoarchitectures exhibited type IV with an H3-type hysteresis loop. The compact pod-like nanoarchitecture 1 (Figure 2d, $D_{104} = 23.3$ nm) had a relatively large adsorbance of N_2 (Figure 3a₁) with a broad hysteresis loop at a relative pressure P/P_0 of 0.45 to 0.95 and a very narrow pore diameter distribution concentrating on 3.8 nm (Figure 3a₂). In contrast, the relative loose pod-like nanoarchitecture 2 (Figure 2e,f, $D_{104} = 27.3$ nm) showed a relatively small adsorbance of N_2 (Figure 3b₁) with a typical H3-type hysteresis loop at a relative pressure P/P_0 of 0.45 to 1.0 and a bimodal pore diameter distribution concentrating on 3.8 and 17.5 nm (Figure 3b₂). The characteristic N_2 adsorption-desorption isotherms (Figure 3a₁, b₁) and pore size distributions (Figure 3a₂, b₂) revealed that both nanoarchitectures 1 and 2 are of mesoporous structures.

Comparatively, the looser pod-like nanoarchitecture 3 (Figure 2g, $D_{104} = 28.0$ nm) demonstrated a similar adsorbance of N_2 (Figure 3c₁) whereas with a narrow hysteresis loop at a relative pressure P/P_0 of 0.40 to 0.95 and a quasi-bimodal pore diameter distribution (Figure 3c₂). Very similarly, the loosest pod-like nanoarchitecture 4 (Figure 2h, $D_{104} = 31.3$ nm) exhibited a relatively low adsorbance of N_2 (Figure 3d₁) with also a narrow hysteresis loop at a relative pressure P/P_0 of 0.25 to 0.95 as well as a quasi-bimodal pore diameter distribution (Figure 3d₂). It was worth noting that the broad hysteresis loop (Figure 3a₁) and relative narrow one (Figure 3b₁) were due to the strong and weak capillarity phenomena existing within the compact (Figure 2d) and relatively loose nanoarchitectures (Figure 2e), respectively. Moreover, the characteristic H3-type hysteresis loop (Figure 3b₁) indicated the existence of dominant slit pores and channels with a relatively uniform shape and size within the relatively loose pod-like nanoarchitectures (Figure 2e,f). This was in accordance with the SEM observation (Figure 1c) and literature results [45,46]. The thin hysteresis loops (Figure 3c₁, d₁) were due to the slight capillarity phenomenon existing within the very loose nanoarchitectures (Figure 2g,h).

As shown in Table 1, with the temperature increasing from 120°C to 150°C, to 180°C, and to 210°C, the corresponding multipoint BET specific surface area of the nanoarchitecture decreased from 21.3 to 5.2, to 2.6, and to 2.0 $m^2 \cdot g^{-1}$, respectively. Meanwhile, the total pore volume changed from 3.9×10^{-2} to 2.9×10^{-2} , to 2.9×10^{-2} , and to 2.1×10^{-2} $cm^3 \cdot g^{-1}$, with a roughly decreasing tendency; the average pore diameter changed from 7.3 to 22.1, to 44.7, and to 40.3 nm, with a roughly increasing tendency. Thus, according to the general recognition of the porous materials [50], nanoarchitectures 3 and 4 were determined as the mesoporous structures, whereas the pore diameters were near the macropores category. As a matter of fact, with the temperature increasing from 120°C to 210°C, the evolution of the BET specific surface area, total pore volume, and average pore diameter of the various-morphology pod-like α - Fe_2O_3 nanoarchitectures agreed with the variation of the D_{104} calculated by the Debye-Scherrer equation, also in accordance with the SEM observation (Figure 2d,e,f,g,h).

Evolution of the hydrothermal products during hydrothermal process

Since the compact pod-like nanoarchitecture obtained at 105°C for 12.0 h (Figure 2c) bridged 1D β - $FeOOH$ nanostructures and pod-like α - Fe_2O_3 nanoarchitectures, the composition and morphology of the products hydrothermally treated at 105°C for various times were monitored, as shown in Figure 4. All hydrothermal products obtained at 105°C for 1.0 to 12.0 h exhibited relatively poor crystallinity (Figure 4a₁, a₂, a₃). When treated for 1.0 h, the product was composed of β - $FeOOH$ (JCPDS No. 34-1266) and detectable trace amount of maghemite (γ - Fe_2O_3 , JCPDS No. 25-1402) in a nearly amorphous state (Figure 4a₁, b). With the time extending to 3.0 h, the product was only β - $FeOOH$ with improved crystallinity, and γ - Fe_2O_3 no longer existed (Figure 4a₂, c). Notably, β - $FeOOH$ at that period exhibited very tiny primary 1D morphology (i.e., fibrils, Figure 4c₁), and a rudimental pod-like aggregate was also observed (denoted as yellow dotted elliptical region in Figure 4c). When treated for 6.0 h, the hydrothermal products containing trace amount of β - $FeOOH$ and majority of newly formed α -

Table 1 Mesoporous structures of the α - Fe_2O_3 synthesized at different temperatures for 12.0 h ($FeCl_3/H_3BO_3/NaOH = 2:3:4$)

α - Fe_2O_3 nanoarchitecture	Temperature (°C)	Multipoint BET ($m^2 \cdot g^{-1}$)	Total pore volume ($cm^3 \cdot g^{-1}$)	Average pore diameter (nm)
1	120	21.3	3.9×10^{-2}	7.3
2	150	5.2	2.9×10^{-2}	22.1
3	180	2.6	2.9×10^{-2}	44.7
4	210	2.0	2.1×10^{-2}	40.3

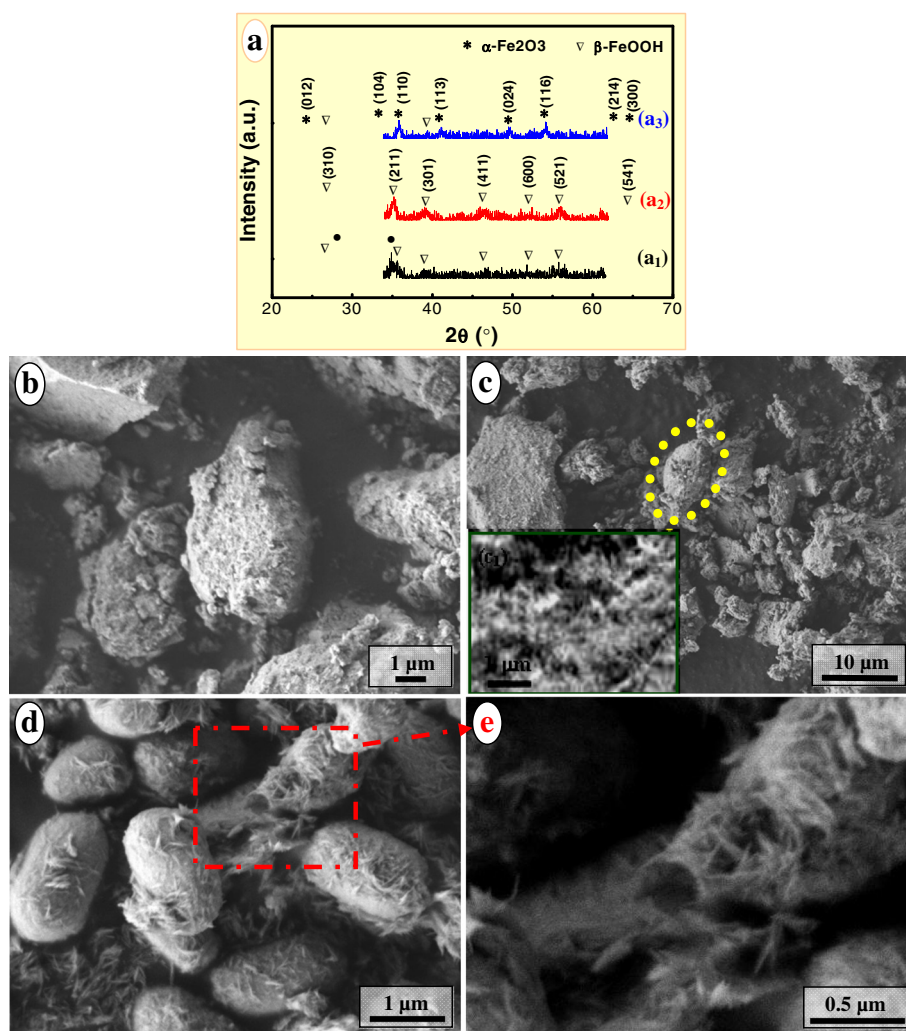


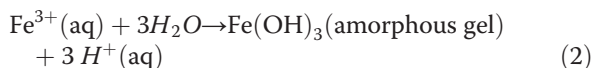
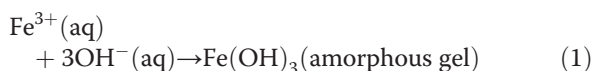
Figure 4 Composition (a) and morphology (b-e) evolution of the hydrothermal products. The products were obtained at 105°C for different times, with the molar ratio of FeCl₃/H₃BO₃/NaOH = 2:3:4. Time (h) = 1.0 (a₁, b); 3.0 (a₂, c); 6.0 (a₃, d, e). The asterisk represents α -Fe₂O₃ (JCPDS No. 33-0664); nabla represents β -FeOOH (JCPDS No. 34-1266); the bullet represents maghemite (γ -Fe₂O₃, JCPDS No. 25-1402). Inset: high-resolution SEM image of the corresponding sample (c₁).

Fe₂O₃ (Figure 4a₃) were acquired, exhibiting pod-like or ellipsoidal-shaped aggregates entangled with 1D nanostructures (Figure 4d). The enlarged image (Figure 4e) corresponding to the red dot-dashed rectangular region in Figure 4d clearly showed that the selected developing pod-like aggregate was assembled by 1D β -FeOOH nanowhiskers. In other words, the pod-like aggregate did not simply coexist or was not simply coated with, but constructed by 1D β -FeOOH nanostructures. With the time prolonged to 12.0 h, as mentioned previously, the pure phase of α -Fe₂O₃ nanoarchitectures consisted of very tiny NPs with compact pod-like and pumpkin-like morphologies acquired (Figure 2a₂,c). The crystallite size D_{104} calculated by the Debye-Scherrer equation was 20.5 nm, smaller than that of the compact pod-like

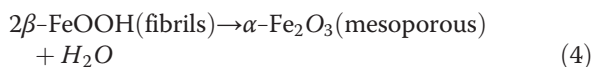
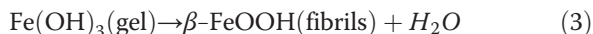
α -Fe₂O₃ nanoarchitectures obtained at 120°C for 12.0 h (Figure 2d) due to a relatively lower temperature hydrothermal treatment.

Formation mechanism of mesoporous pod-like α -Fe₂O₃ nanoarchitectures

From the phase conversion and morphology evolution of the hydrothermal products, formation of the monodisperse pod-like α -Fe₂O₃ phase could be further clarified, which experienced a two-step phase transformation from Fe(OH)₃ to β -FeOOH and from β -FeOOH to α -Fe₂O₃ [51,52]. The room-temperature coprecipitation of FeCl₃ and NaOH solutions and hydrolysis of excessive Fe³⁺ ions can be expressed as



Hydrothermal conversion of amorphous $\text{Fe}(\text{OH})_3$ gel can be expressed as



As known, iron oxyhydroxides (FeOOH) can be crystallized as goethite ($\alpha\text{-FeOOH}$), lepidocrocite ($\gamma\text{-FeOOH}$), and akaganeite ($\beta\text{-FeOOH}$), and an environment rich of Cl^{-} was favorable for the formation of $\beta\text{-FeOOH}$ phase [53]. In the present case, a molar ratio of the reactants as $\text{FeCl}_3/\text{H}_3\text{BO}_3/\text{NaOH} = 2:(0-3):4$ led to a surrounding rich of Cl^{-} and thus promoted the formation of $\beta\text{-FeOOH}$. Tiny $\beta\text{-FeOOH}$ fibrils with poor crystallinity formed at the early stage of the hydrothermal treatment (e.g., 90°C , 12.0 h, Figure 2a₁; 105°C , 1.0 to 3.0 h, Figure 4a₁,a₂) tended to agglomerate with each other owing to the high surface energy, leading to quasi-amorphous agglomerate bulks of irregular shape (Figures 2b and 4b,c). Undoubtedly, the conversion from $\beta\text{-FeOOH}$ to $\alpha\text{-Fe}_2\text{O}_3$ was crucial to the formation of mesoporous pod-like hematite nanoarchitectures. Sugimoto et al. reported a preparation of monodisperse peanut-type $\alpha\text{-Fe}_2\text{O}_3$ particles from condensed ferric hydroxide gel in the presence of sulfate [49] and found that ellipsoidal hematite turned into a peanut-like shape with the increase in the concentration of sulfate [51]. In the present case, although quasi-spherical $\alpha\text{-Fe}_2\text{O}_3$ NPs were obtained in due case (Figure 1b), the mesoporous hematite nanoarchitectures (Figures 1c,d,e,f and 2d,e,f,g,h) were not directly assembled by those NPs, taking into consideration the remarkable differences of the morphology especially size between the NPs and subunits of nanoarchitectures. It was worth noting that the hydrothermally formed hematite particles exhibited a peanut-like shape at the molar ratio of $\text{FeCl}_3/\text{H}_3\text{BO}_3/\text{NaOH}$ as 2:0:2 (Figure 1d) and a pod-like shape at the molar ratio of $\text{FeCl}_3/\text{H}_3\text{BO}_3/\text{NaOH}$ as 2:(0-3):4 (Figures 1c,e,f and 2d,e,f,g,h). Moreover, with the content of H_3BO_3 increasing, the pod-like $\alpha\text{-Fe}_2\text{O}_3$ nanoarchitectures tended to be uniform in size distribution. Consequently, the morphology evolution of the hydrothermally synthesized $\alpha\text{-Fe}_2\text{O}_3$ nanoarchitectures in the presence of boric acid, from a peanut-type to a pod-like shape, was obviously different from that of the peanut-type $\alpha\text{-Fe}_2\text{O}_3$ particles that originated from condensed ferric hydroxide gel in the presence of sulfate [49].

Thus, based on the present experimental results (Figures 1, 2, 3, and 4), the overall formation mechanism of mesoporous pod-like hematite nanoarchitectures in the presence of boric acid was illustrated in Figure 5. Firstly, the amorphous $\text{Fe}(\text{OH})_3$ gel derived from room-temperature coprecipitation was hydrothermally treated under an environment rich of Cl^{-} , leading to poor-crystallinity $\beta\text{-FeOOH}$ fibrils (Figure 5a) [53]. Secondly, with the hydrothermal temperature going up and time going on, $\beta\text{-FeOOH}$ fibrils were organized into a peanut-type assembly, and at the same time, $\beta\text{-FeOOH}$ fibrils began to dissolve, resulting in $\alpha\text{-Fe}_2\text{O}_3$ NPs. As a consequence, peanut-like $\beta\text{-FeOOH}/\alpha\text{-Fe}_2\text{O}_3$ assemblies were obtained (Figure 5b). This process was very analogous to the 'rod-to-dumbbell-to-sphere' transformation phenomenon, which had been found in the formation of some other hierarchical architectures, such as carbonates (CaCO_3 , BaCO_3 , SrCO_3 , MnCO_3 , CdCO_3) [8,54,55], fluoroapatite ($\text{Ca}_5(\text{PO}_4)_3\text{OH}$) [56], etc. Like the dumbbell transition structure, the present peanut-type assembly was also believed to be formed due to the reaction-limited aggregation. Thirdly, with the hydrothermal treatment further going on, remanent $\beta\text{-FeOOH}$ fibrils were further dissolved and the peanut-like $\beta\text{-FeOOH}/\alpha\text{-Fe}_2\text{O}_3$ assemblies were converted into relatively compact pod-like $\alpha\text{-Fe}_2\text{O}_3$ nanoarchitectures, consisting of 1D or linear chain-like assemblies of rod-like subcrystals or tiny NPs within the body (Figure 5c). No proof convinced that the peanut-type $\beta\text{-FeOOH}/\alpha\text{-Fe}_2\text{O}_3$ assemblies were thoroughly dissolved and reorganized into the pod-like nanoarchitectures with almost unchanged external shape and size. In other words, peanut-like $\beta\text{-FeOOH}/\alpha\text{-Fe}_2\text{O}_3$ assemblies were *in situ* transformed into $\alpha\text{-Fe}_2\text{O}_3$ NPs within the peanut-like aggregates owing to the hydrothermal treatment. However, the *in situ* converted tiny $\alpha\text{-Fe}_2\text{O}_3$ NPs bore high surface energy. This promoted the aggregation, instead of the segregation, of those tiny NPs so as to reduce the overall surface energy, leading to relatively compact pod-like $\alpha\text{-Fe}_2\text{O}_3$ nanoarchitectures due to a slight expansion of the entire volume. Finally, with the hydrothermal treatment going on, the compact pod-like $\alpha\text{-Fe}_2\text{O}_3$ nanoarchitectures became looser and looser owing to the coarsening [57,58] of the constitutional NPs controlled by the traditional Ostwald ripening, i.e., dissolution-reprecipitation mechanism (Figure 5d) [58]. The constitutional $\alpha\text{-Fe}_2\text{O}_3$ subcrystals grew into larger NPs, with 1D assembly behavior disappeared largely.

It is notable, however, that the boric acid played a significant role in the formation of the present mesoporous pod-like $\alpha\text{-Fe}_2\text{O}_3$ nanoarchitectures with uniform morphology and size, confirmed by the above experimental results (Figures 1 and 2). Also, as confirmed to improve the uniformity, the amount of boric acid or molar ratio of $\text{FeCl}_3/\text{H}_3\text{BO}_3/\text{NaOH}$ should be tuned within a certain composition range. As known, as a weak acid, H_3BO_3

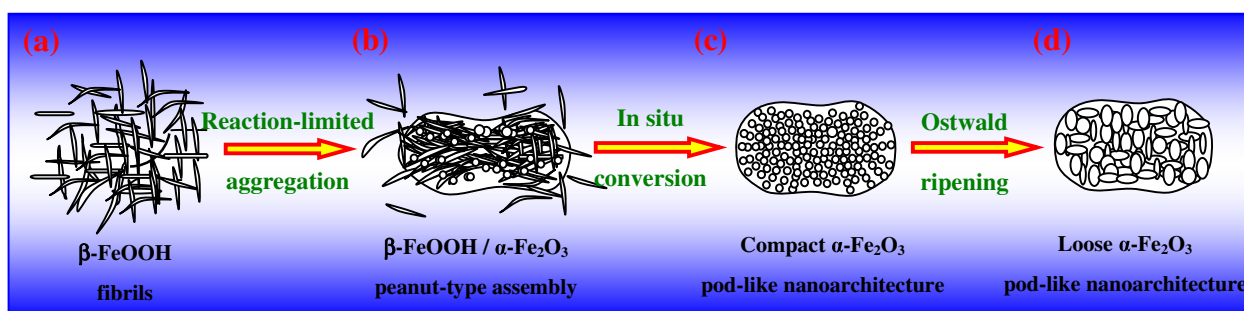


Figure 5 Formation mechanism of the hierarchical mesoporous pod-like hematite nanoarchitectures.

could form sodium borate (i.e., borax) after the introduction of NaOH, giving rise to the buffer solution. This could tune the release of hydroxyl ions and further control the mild formation of amorphous $\text{Fe}(\text{OH})_3$ gel, leading to subsequent $\beta\text{-FeOOH}$ fibrils with relatively uniform size. This was believed to contribute to the further formation of the peanut-like $\beta\text{-FeOOH}/\alpha\text{-Fe}_2\text{O}_3$ assemblies and ultimate occurrence of the pod-like $\alpha\text{-Fe}_2\text{O}_3$ nanoarchitectures.

Optical absorbance analysis

Hematite NPs have been widely used as ultraviolet absorbents for their broad absorption in the ultraviolet region from the electron transition of Fe-O. Figure 6 shows the optical absorbance spectra of the $\alpha\text{-Fe}_2\text{O}_3$ particles with the photon wavelength in the range of 350

to 650 nm. For sample a_1 , it revealed two absorption edges around 380 to 450 and 540 to 560 nm, which were consistent with the reported hematite NPs [59-61]. When the $\alpha\text{-Fe}_2\text{O}_3$ clustered into samples b_1 and c_1 , the size of $\alpha\text{-Fe}_2\text{O}_3$ agglomerates was around 500 to 800 nm. The absorbance spectra showed two absorption peaks around 520 to 570 and 600 to 640 nm. The change in the degree of transition depended on the shape and size of the particles. When the hematite particles aggregated to pod-like nanoarchitectures, the size became larger, and then the scattering of visible light was superimposed on the absorption of as-prepared architectures.

It was well illustrated that three types of electronic transitions occurred in the optical absorption spectra of

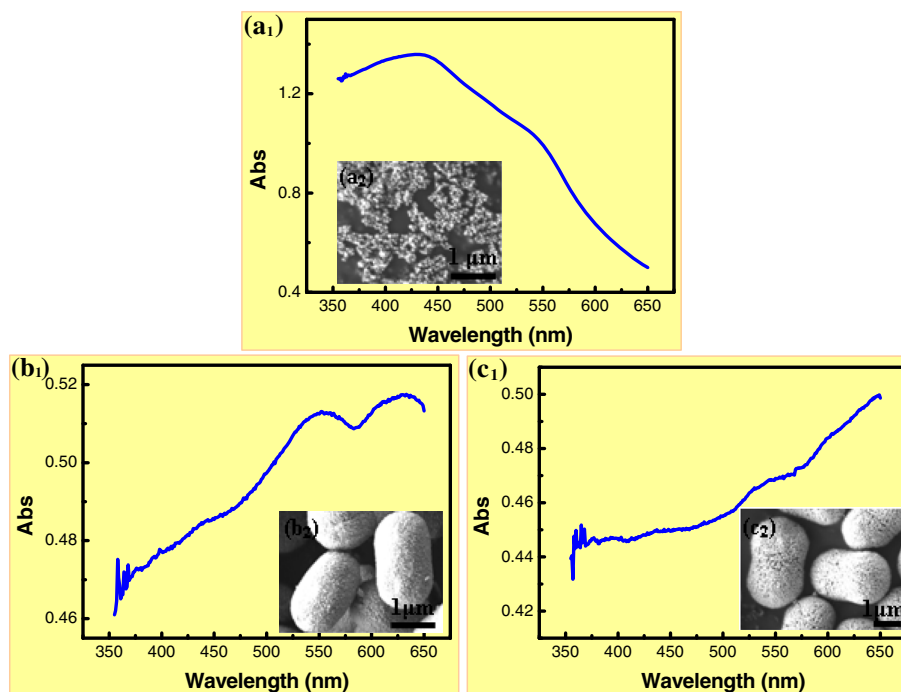


Figure 6 Optical absorbance spectra (a_1 - c_1) of the $\alpha\text{-Fe}_2\text{O}_3$ with different morphologies (a_2 - c_2). Time (h) = 12.0; Temperature ($^{\circ}\text{C}$) = 120 (a_1 , a_2 , b_1 , b_2), 150 (c_1 , c_2); $\text{FeCl}_3/\text{H}_3\text{BO}_3/\text{NaOH}$ = 2:3:6 (a_1 , a_2), 2:3:4 (b_1 , b_2 , c_1 , c_2).

Fe^{3+} substances: (a) the Fe^{3+} ligand field transition or the $d-d$ transitions, (b) the ligand to metal charge-transfer transitions, and (c) the pair excitations resulting from the simultaneous excitations of two neighboring Fe^{3+} cations that are magnetically coupled. According to [62,63], the absorption bands near 390 and 430 nm corresponded to the ${}^6\text{A}_1 \rightarrow {}^4\text{E}({}^4\text{G})$ and ${}^6\text{A}_1 \rightarrow {}^4\text{E}, {}^4\text{A}_1({}^4\text{G})$ ligand field transitions of Fe^{3+} [59,60]. The observed edge at around 520 to 570 and 600 to 640 nm could be assigned to the ${}^6\text{A}_1 \rightarrow {}^4\text{T}_2({}^4\text{G})$ ligand field transition of Fe^{3+} . As revealed by Figure 6, the electronic transition for the charge transfer in the wavelength region 380 to 450 nm dominated the optical absorption features of the NPs, while the ligand field transitions in the range of 520 to 640 nm dominated the optical absorption features

of the architectures. This indicated that the absorption could be modulated by controlling the size and shape of the hematite, which was quite important for the enhancement of the photoelectrocatalytic activity.

Mesoporous pod-like $\alpha\text{-Fe}_2\text{O}_3$ nanoarchitectures as anode materials for lithium-ion batteries

The electrochemical behavior of the hematite electrodes was evaluated by cyclic voltammetry and galvanostatic charge/discharge cycling. As shown in Figure 7a, a spiky peak was observed at 0.65 V with a small peak appearing at 1.0 V during the cathodic polarization of the hematite NPs (presented in Figure 1b) in the first cycle. This indicated the following lithiation steps [43,64,65]:

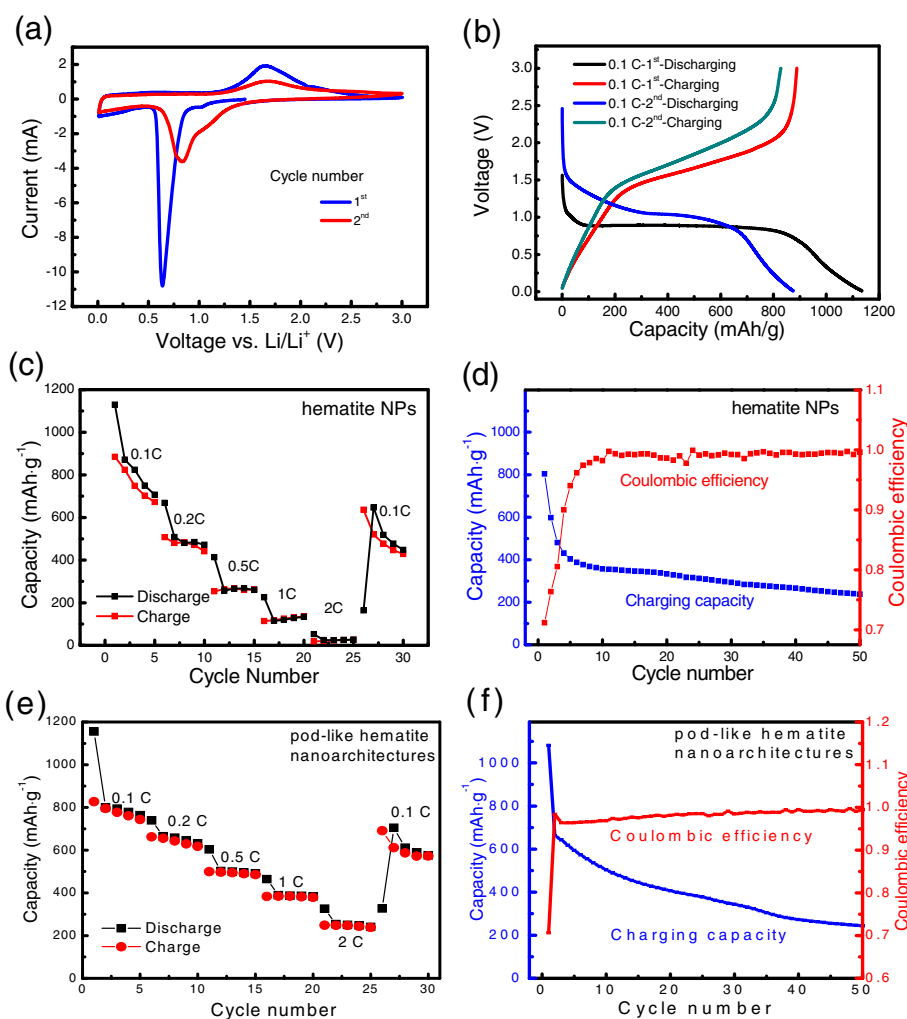
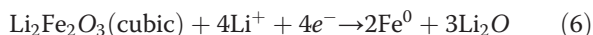
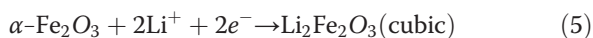


Figure 7 Representative cyclic voltammograms and charge-discharge performances of the hematite electrode. (a) Representative cyclic voltammograms of the hematite nanoparticles (presented in Figure 1b) at a scan rate of 0.1 mV s⁻¹; (b) the charge-discharge performances at various current rates (1 C = 1,006 mA g⁻¹, corresponding to the full discharge in 1 h, a rate of n C corresponds to the full discharge in $1/n$ h) of the hematite nanoparticles; (c) the rate performance and (d) the cycling performance at a current of 1 C of an electrode fabricated with the hematite nanoparticles presented in Figure 1b; (e) the rate performance and (f) the cycling performance at a current of 1 C of an electrode fabricated with hierarchical mesoporous pod-like hematite nanoarchitectures presented in Figure 2e.



With lithium ions inserted into the crystal structure of the as-prepared $\alpha\text{-Fe}_2\text{O}_3$, the hexagonal $\alpha\text{-Fe}_2\text{O}_3$ was transformed to cubic $\text{Li}_2\text{Fe}_2\text{O}_3$. The peak at 0.65 V corresponded to the complete reduction of iron from Fe^{2+} to Fe^0 and the decomposition of electrolyte. A broad anodic peak was recorded in the range of 1.4 to 2.2 V, corresponding to the oxidation of Fe^0 to Fe^{2+} and further to Fe^{3+} [66,67]. The curve of the subsequent cycle was significantly different from that of the first cycle as only one cathodic peak appeared at about 0.8 V with decreased peak intensity, while the anodic process only showed one broad peak with a little decrease in peak intensity. The irreversible phase transformation during the process of lithium insertion and extraction in the initial cycle was the reason for the difference between the first and second cathodic curves [24]. After the first discharge process, $\alpha\text{-Fe}_2\text{O}_3$ was completely reduced to iron NPs and was dispersed in a Li_2O matrix. The decrease of the redox peak intensity implied that the capacity was decreased during cycling.

The charge–discharge curves of the $\alpha\text{-Fe}_2\text{O}_3$ NP (shown in Figure 1b) electrode during the first and second cycles are shown in Figure 7b. In the first discharge curve, there was a weak potential slope located at 1.2 to 1.0 V and an obvious potential plateau at 0.9 to 0.8 V. The capacity obtained above 0.8 V was $780 \text{ mAh}\cdot\text{g}^{-1}$ (4.6 mol of Li per mole of $\alpha\text{-Fe}_2\text{O}_3$). After discharging to 0.01 V, the total specific capacity of the as-prepared $\alpha\text{-Fe}_2\text{O}_3$ reached $887 \text{ mAh}\cdot\text{g}^{-1}$, corresponding to 5.3 mol of Li per mole of $\alpha\text{-Fe}_2\text{O}_3$. During the second cycle, the discharge curve only showed a slope at 1.0 to 0.8 V, and the capacity was reduced to $824 \text{ mAh}\cdot\text{g}^{-1}$. Usually, the slope behavior during the discharge process of metal oxide anode materials was considered to be related with the irreversible formation of a nanocomposite of crystalline grains of metals and amorphous Li_2O matrix.

The comparison of the rate as well as cycling performances between Fe_2O_3 NPs and nanoarchitectures were also conducted, which were obtained by a 12.0-h hydrothermal treatment at 150°C with a molar ratio of $\text{FeCl}_3/\text{H}_3\text{BO}_3/\text{NaOH}$ as 2:0:4 (Figure 1b) and 2:3:4 (Figure 2e), respectively. The discharge and charge capacities in the first cycle at a current of 0.1 C were 1,129 and $887 \text{ mAh}\cdot\text{g}^{-1}$ for Fe_2O_3 NPs (Figure 7c) and 1,155 and $827 \text{ mAh}\cdot\text{g}^{-1}$ for Fe_2O_3 nanoarchitectures. For the second cycle, the discharge and charge capacities were 871 and $824 \text{ mAh}\cdot\text{g}^{-1}$ for Fe_2O_3 NPs and 799 and $795 \text{ mAh}\cdot\text{g}^{-1}$ for Fe_2O_3 nanoarchitectures. The Li-ion storage capacitance of the current Fe_2O_3 NPs/nanoarchitectures

reported in this work is higher than that of hematite nanorod (*ca.* $400 \text{ mAh}\cdot\text{g}^{-1}$ at 0.1 C) [68], nanoflakes [69], hierarchical mesoporous hematite (*ca.* $700 \text{ mAh}\cdot\text{g}^{-1}$ at 0.1 C) [65], hollow nanospindles ($457 \text{ mAh}\cdot\text{g}^{-1}$ at 0.2 mA cm^{-2}) [37], hollow microspheres ($621 \text{ mAh}\cdot\text{g}^{-1}$ at 0.2 mA cm^{-2}) [37], and dendrites ($670 \text{ mAh}\cdot\text{g}^{-1}$ at 1 mA cm^{-2}) [70]. When the current increased, both the discharge and charge capacities decreased, especially for Fe_2O_3 NPs (Figure 7c,e). The discharge and charge capacities of Fe_2O_3 nanoarchitectures were larger than those of Fe_2O_3 NPs. For instance, when the current rate increased to 2.0 C, the charge and discharge capacities of Fe_2O_3 nanoarchitectures were 253 and $247 \text{ mAh}\cdot\text{g}^{-1}$, while those of Fe_2O_3 NPs were only 24 and $21 \text{ mAh}\cdot\text{g}^{-1}$. This indicated that the Fe_2O_3 nanoarchitectures presented much improved rate performance for the reason that the porous nature of Fe_2O_3 nanoarchitectures allow a fast Li-ion diffusion by offering better electrolyte accessibility and also accommodate the volume change of NPs during Li insertion/extraction.

However, similar to many Fe_2O_3 nanostructures reported in literatures, the $\alpha\text{-Fe}_2\text{O}_3$ nanoarchitectures exhibited a rapid capacity fading within the potential range of 0.01 to 3.0 V, suggesting that the crystalline structure of the electrode materials was destroyed by the insertion/extraction of lithium ions and the electrode decomposed the electrolyte. The Fe_2O_3 nanoarchitectures presented superior charge/discharge stability to the Fe_2O_3 NPs, e.g., the charging capacities of Fe_2O_3 nanoarchitectures (Figure 7f) and NPs (Figure 7d) of the tenth cycle were 503 and $356 \text{ mAh}\cdot\text{g}^{-1}$, respectively. This indicated that the mesoporous structure of Fe_2O_3 nanoarchitectures provided more space for Fe_2O_3 volume change and avoided severe pulverization. Such an improvement could also be confirmed by the cycling performance of mesoporous hematite [67], which maintained a good stability attributed from the small Fe_2O_3 size (*ca.* 10 nm) and abundant pores. The introduction of conductive carbon into the hematite electrode is an effective way to improve the cycle performance [68]. It is highly expected that the hierarchical Fe_2O_3 nanoarchitectures with ultrafine Fe_2O_3 building blocks and interconnected pores afford shorter Li-ion diffusion way, fast diffusion rate, and large-volume changes during the charge/discharge process, which can serve as potential anode materials for Li-ion storage.

Conclusions

Uniform monodisperse hierarchical $\alpha\text{-Fe}_2\text{O}_3$ nanoarchitectures with a pod-like shape have been synthesized via a facile, environmentally benign, and low-cost hydrothermal method (120°C to 210°C , 12.0 h), by using $\text{FeCl}_3\cdot 6\text{H}_2\text{O}$ and NaOH as raw materials in the presence of H_3BO_3 (molar ratio, $\text{FeCl}_3/\text{H}_3\text{BO}_3/\text{NaOH} = 2:3:4$).

The mesoporous α -Fe₂O₃ nanoarchitectures had a specific surface area of 21.3 to 5.2 m²·g⁻¹ and an average pore diameter of 7.3 to 22.1 nm. The mesoporous α -Fe₂O₃ nanoarchitectures were formed as follows: the reaction-limited aggregation of β -FeOOH fibrils led to β -FeOOH/ α -Fe₂O₃ peanut-type assembly, which was subsequently and *in situ* converted into compact pod-like α -Fe₂O₃ nanoarchitectures and further into loose pod-like α -Fe₂O₃ nanoarchitectures through a high-temperature, long-time hydrothermal treatment via the Ostwald ripening. Benefiting from their unique structural characteristics, the as-synthesized hierarchical mesoporous pod-like α -Fe₂O₃ nanoarchitectures exhibited good absorbance and a high specific discharge capacity. Compared with the traditional solid-state monomorph hematite NPs and other complicated porous hematite nanoarchitectures, the as-synthesized hierarchical mesoporous pod-like α -Fe₂O₃ nanoarchitectures derived from the facile, environmentally benign, and low-cost hydrothermal route can provide an alternative candidate for novel applications in booming fields, such as gas sensors, lithium-ion batteries, photocatalysis, water treatment, and photoelectrochemical water splitting.

Competing interests

The authors declare that they have no competing interests.

Authors' contributions

WCZ provided guidance to XLC, XFL, and LYZ as he was the supervisor. WCZ and QZ wrote the paper. JQH conducted the research study on the Li-ion storage performance test. XLP conducted the surface area measurement. All authors read and approved the final manuscript.

Acknowledgements

This work was supported by the National Natural Science Foundation of China (no. 21276141), the State Key Laboratory of Chemical Engineering, China (no. SKL-ChE-12A05), a project of Shandong Province Higher Educational Science and Technology Program, China (J10LB15), and the Excellent Middle-Aged and Young Scientist Award Foundation of Shandong Province, China (BS2010CL024).

Received: 16 July 2012 Accepted: 2 December 2012

Published: 2 January 2013

References

1. Fan HJ, Werner P, Zacharias M: Semiconductor nanowires: from self-organization to patterned growth. *Small* 2006, **2**:700–717.
2. Shang M, Wang WZ, Ren J, Sun SM, Zhang L: A novel BiVO₄ hierarchical nanostructure: controllable synthesis, growth mechanism, and application in photocatalysis. *Cryst Eng Comm* 2010, **12**:1754–1758.
3. Zhao MQ, Zhang Q, Huang JQ, Wei F: Hierarchical nanocomposites derived from nanocarbons and layered double hydroxides - properties, synthesis, and applications. *Adv Funct Mater* 2012, **22**:675–694.
4. Colfen H, Antonietti M: Mesocrystals: inorganic superstructures made by highly parallel crystallization and controlled alignment. *Angew Chem Int Ed* 2005, **44**:5576–5591.
5. Song RQ, Colfen H: Mesocrystals - ordered nanoparticle superstructures. *Adv Mater* 2010, **22**:1301–1330.
6. Liu J, Liu F, Gao K, Wu JS, Xue DF: Recent developments in the chemical synthesis of inorganic porous capsules. *J Mater Chem* 2009, **19**:6073–6084.
7. Zhong SL, Song JM, Zhang S, Yao HB, Xu AW, Yao WT, Yu SH: Template-free hydrothermal synthesis and formation mechanism of hematite microrings. *J Phys Chem C* 2008, **112**:19916–19921.
8. Zhu WC, Zhang GL, Li J, Zhang Q, Piao XL, Zhu SL: Hierarchical mesoporous SrCO₃ submicron spheres derived from reaction-limited aggregation induced "rod-to-dumbbell-to-sphere" self-assembly. *Cryst Eng Comm* 2010, **12**:1795–1802.
9. Byrappa K, Adschiri T: Hydrothermal technology for nanotechnology. *Prog Cryst Growth Ch* 2007, **53**:117–166.
10. Yoshimura M, Byrappa K: Hydrothermal processing of materials: past, present and future. *J Mater Sci* 2008, **43**:2085–2103.
11. Shahmoradi B, Soga K, Ananda S, Somashekar R, Byrappa K: Modification of neodymium-doped ZnO hybrid nanoparticles under mild hydrothermal conditions. *Nanoscale* 2010, **2**:1160–1164.
12. Neira IS, Kolen'ko YV, Lebedev OI, Van Tendeloo G, Gupta HS, Guitian F, Yoshimura M: An effective morphology control of hydroxyapatite crystals via hydrothermal synthesis. *Cryst Growth Des* 2009, **9**:466–474.
13. Feng YL, Lu WC, Zhang LM, Bao XH, Yue BH, Iv Y, Shang XF: One-step synthesis of hierarchical cantaloupe-like AlOOH superstructures via a hydrothermal route. *Cryst Growth Des* 2008, **8**:1426–1429.
14. Shao YZ, Sun J, Gao L: Hydrothermal synthesis of hierarchical nanocolumns of cobalt hydroxide and cobalt oxide. *J Phys Chem C* 2009, **113**:6566–6572.
15. Cao F, Shi WD, Zhao LJ, Song SY, Yang JH, Lei YQ, Zhang HJ: Hydrothermal synthesis and high photocatalytic activity of 3D wurtzite ZnSe hierarchical nanostructures. *J Phys Chem C* 2008, **112**:17095–17101.
16. Kuang DB, Lei BX, Pan YP, Yu XY, Su CY: Fabrication of novel hierarchical β -Ni(OH)₂ and NiO microspheres via an easy hydrothermal process. *J Phys Chem C* 2009, **113**:5508–5513.
17. Agarwala S, Lim ZH, Nicholson E, Ho GW: Probing the morphology-device relation of Fe₂O₃ nanostructures towards photovoltaic and sensing applications. *Nanoscale* 2012, **4**:194–205.
18. Sivula K, Le Formal F, Gratzel M: Solar water splitting: progress using hematite (α -Fe₂O₃) photoelectrodes. *Chem Sus Chem* 2011, **4**:432–449.
19. Cheng CJ, Lin CC, Chiang RK, Lin CR, Lyubutin IS, Alkaev EA, Lai HY: Synthesis of monodisperse magnetic iron oxide nanoparticles from submicrometer hematite powders. *Cryst Growth Des* 2008, **8**:877–883.
20. Wu CZ, Yin P, Zhu X, OuYang CZ, Xie Y: Synthesis of hematite (α -Fe₂O₃) nanorods: diameter-size and shape effects on their applications in magnetism, lithium ion battery, and gas sensors. *J Phys Chem B* 2006, **110**:17806–17812.
21. Wu ZC, Yu K, Zhang SD, Xie Y: Hematite hollow spheres with a mesoporous shell: controlled synthesis and applications in gas sensor and lithium ion batteries. *J Phys Chem C* 2008, **112**:11307–11313.
22. Kim HS, Piao Y, Kang SH, Hyeon T, Sung YE: Uniform hematite nanocapsules based on an anode material for lithium ion batteries. *Electrochem Commun* 2010, **12**:382–385.
23. Ma JM, Lian JB, Duan XC, Liu XD, Zheng WJ: α -Fe₂O₃: hydrothermal synthesis, magnetic and electrochemical properties. *J Phys Chem C* 2010, **114**:10671–10676.
24. Wang ZY, Luan DY, Madhavi S, Li CM, Lou XW: α -Fe₂O₃ nanotubes with superior lithium storage capability. *Chem Commun* 2011, **47**:8061–8063.
25. Chen JS, Zhu T, Yang XH, Yang HG, Lou XW: Top-down fabrication of α -Fe₂O₃ single-crystal nanodiscs and microparticles with tunable porosity for largely improved lithium storage properties. *J Am Chem Soc* 2010, **132**:13162–13164.
26. Muruganandham M, Amutha R, Sathish M, Singh TS, Suri RPS, Sillanpaa M: Facile fabrication of hierarchical α -Fe₂O₃: self-assembly and its magnetic and electrochemical properties. *J Phys Chem C* 2011, **115**:18164–18173.
27. Liu JP, Li YY, Fan HJ, Zhu ZH, Jiang J, Ding RM, Hu YY, Huang XT: Iron oxide-based nanotube arrays derived from sacrificial template-accelerated hydrolysis: large-area design and reversible lithium storage. *Chem Mater* 2010, **22**:212–217.
28. Brezesinski K, Haetge J, Wang J, Mascotto S, Reitz C, Rein A, Tolbert SH, Perlich J, Dunn B, Brezesinski T: Ordered mesoporous α -Fe₂O₃ (hematite) thin-film electrodes for application in high rate rechargeable lithium batteries. *Small* 2011, **7**:407–414.
29. Li L, Koshizaki N: Vertically aligned and ordered hematite hierarchical columnar arrays for applications in field-emission, superhydrophilicity, and photocatalysis. *J Mater Chem* 2010, **20**:2972–2978.
30. LaTempa TJ, Feng XJ, Paulose M, Grimes CA: Temperature-dependent growth of self-assembled hematite (α -Fe₂O₃) nanotube arrays: rapid electrochemical synthesis and photoelectrochemical properties. *J Phys Chem C* 2009, **113**:16293–16298.
31. Tsuzuki T, Schaffel F, Muroi M, McCormick PG: α -Fe₂O₃ nano-platelets prepared by mechanochemical/thermal processing. *Powder Technol* 2011, **210**:198–202.

32. An ZG, Zhang JJ, Pan SL, Song GZ: Novel peanut-like α -Fe₂O₃ superstructures: oriented aggregation and Ostwald ripening in a one-pot solvothermal process. *Powder Technol* 2012, **217**:274–280.
33. Zhu LP, Xiao HM, Fu SY: Template-free synthesis of monodispersed and single-crystalline cantaloupe-like Fe₂O₃ superstructures. *Cryst Growth Des* 2007, **7**:177–182.
34. Zeng SY, Tang KB, Li TW, Liang ZH: Hematite with the urchinlike structure: its shape-selective synthesis, magnetism, and enhanced photocatalytic performance after TiO₂ encapsulation. *J Phys Chem C* 2010, **114**:274–283.
35. Gong CR, Chen DR, Jiao XL, Wang QL: Continuous hollow α -Fe₂O₃ and α -Fe fibers prepared by the sol-gel method. *J Mater Chem* 2002, **12**:1844–1847.
36. Bang JH, Suslick KS: Sonochemical synthesis of nanosized hollow hematite. *J Am Chem Soc* 2007, **129**:2242–2243.
37. Zeng SY, Tang KB, Li TW, Liang ZH, Wang D, Wang YK, Zhou WW: Hematite hollow spindles and microspheres: selective synthesis, growth mechanisms, and application in lithium ion battery and water treatment. *J Phys Chem C* 2007, **111**:10217–10225.
38. Li X, Yu X, He JH, Xu Z: Controllable fabrication, growth mechanisms, and photocatalytic properties of hematite hollow spindles. *J Phys Chem C* 2009, **113**:2837–2845.
39. Kandori K, Okamoto N, Ishikawa T: Preparation of nanoporous micrometer-scale hematite particles by a forced hydrolysis reaction in the presence of polyethylene glycol. *Langmuir* 2002, **18**:2895–2900.
40. Kandori K, Hori N, Ishikawa T: Preparation of mesoporous hematite particles by a forced hydrolysis reaction accompanying a peptide production reaction. *Colloids Surf A* 2006, **290**:280–287.
41. Sivula K, Zboril R, Le Formal F, Robert R, Weidenkaff A, Tucek J, Frydrych J, Gratzel M: Photoelectrochemical water splitting with mesoporous hematite prepared by a solution-based colloidal approach. *J Am Chem Soc* 2010, **132**:7436–7444.
42. Fang XL, Chen C, Jin MS, Kuang Q, Xie ZX, Xie SY, Huang RB, Zheng LS: Single-crystal-like hematite colloidal nanocrystal clusters: synthesis and applications in gas sensors, photocatalysis and water treatment. *J Mater Chem* 2009, **19**:6154–6160.
43. Zeng SY, Tang KB, Li TW, Liang ZH, Wang D, Wang YK, Qi YX, Zhou WW: Facile route for the fabrication of porous hematite nanoflowers: its synthesis, growth mechanism, application in the lithium ion battery, and magnetic and photocatalytic properties. *J Phys Chem C* 2008, **112**:4836–4843.
44. Zhu WC, Cui XL, Wang L, Liu T, Zhang Q: Monodisperse porous pod-like hematite: hydrothermal formation, optical absorbance, and magnetic properties. *Mater Lett* 2011, **65**:1003–1006.
45. Shindo D, Park GS, Waseda Y, Sugimoto T: Internal structure-analysis of monodispersed peanut-type hematite particles produced by the gel-sol method. *J Colloid Interf Sci* 1994, **168**:478–484.
46. Žic M, Ristić M, Musić S: Precipitation of α -Fe₂O₃ from dense β -FeOOH suspensions with added ammonium amidosulfonate. *J Mol Struct* 2009, **924**:235–242.
47. Sugimoto T, Itoh H, Mochida T: Shape control of monodisperse hematite particles by organic additives in the gel-sol system. *J Colloid Interf Sci* 1998, **205**:42–52.
48. Sugimoto T, Wang YS, Itoh H, Muramatsu A: Systematic control of size, shape and internal structure of monodisperse α -Fe₂O₃ particles. *Colloids Surf A* 1998, **134**:265–279.
49. Sugimoto T, Khan MM, Muramatsu A: Preparation of monodisperse peanut-type α -Fe₂O₃ particles from condensed ferric hydroxide gel. *Colloids Surf A* 1993, **70**:167–169.
50. Davis ME: Ordered porous materials for emerging applications. *Nature* 2002, **417**:813–821.
51. Sugimoto T, Khan MM, Muramatsu A, Itoh H: Formation mechanism of monodisperse peanut-type α -Fe₂O₃ particles from condensed ferric hydroxide gel. *Colloids Surf A* 1993, **79**:233–247.
52. Almeida TP, Fay MW, Zhu YQ, Brown PD: Hydrothermal growth mechanism of α -Fe₂O₃ nanorods derived by near *in situ* analysis. *Nanoscale* 2010, **2**:2390–2399.
53. Bakoyannakis DN, Deliyanni EA, Zouboulis AI, Matis KA, Nalbandian L, Kehagias T: Akaganeite and goethite-type nanocrystals: synthesis and characterization. *Micropor Mesopor Mat* 2003, **59**:35–42.
54. Raz S, Weiner S, Addadi L: Formation of high-magnesian calcites via an amorphous precursor phase: possible biological implications. *Adv Mater* 2000, **12**:38–42.
55. Yu SH, Colfen H, Antonietti M: Polymer-controlled morphosynthesis and mineralization of metal carbonate superstructures. *J Phys Chem B* 2003, **107**:7396–7405.
56. Kniep R, Busch S: Biomimetic growth and self-assembly of fluorapatite aggregates by diffusion into denatured collagen matrices. *Angew Chem Int Ed Engl* 1996, **35**:2624–2626.
57. Baldan A: Review progress in Ostwald ripening theories and their applications to nickel-base superalloys - part I: Ostwald ripening theories. *J Mater Sci* 2002, **37**:2171–2202.
58. Oskam G, Hu ZS, Penn RL, Pesika N, Searson PC: Coarsening of metal oxide nanoparticles. *Phys Rev E* 2002, **66**:011403.
59. Lian JB, Duan XC, Ma JM, Peng P, Kim TI, Zheng WJ: Hematite (α -Fe₂O₃) with various morphologies: ionic liquid-assisted synthesis, formation mechanism, and properties. *ACS Nano* 2009, **3**:3749–3761.
60. Mitra S, Das S, Mandal K, Chaudhuri S: Synthesis of a α -Fe₂O₃ nanocrystal in its different morphological attributes: growth mechanism, optical and magnetic properties. *Nanotechnology* 2007, **18**:275608.
61. Zhang ZH, Hossain MF, Takahashi T: Self-assembled hematite (α -Fe₂O₃) nanotube arrays for photoelectrocatalytic degradation of azo dye under simulated solar light irradiation. *Appl Catal B Environ* 2010, **95**:423–429.
62. He YP, Miao YM, Li CR, Wang SQ, Cao L, Xie SS, Yang GZ, Zou BS, Burda C: Size and structure effect on optical transitions of iron oxide nanocrystals. *Phys Rev B* 2005, **71**:125411.
63. Hashimoto T, Yamada T, Yoko T: Third-order nonlinear optical properties of sol-gel derived α -Fe₂O₃, γ -Fe₂O₃, and Fe₃O₄ thin films. *J Appl Phys* 1996, **80**:3184–3190.
64. Larcher D, Masquelier C, Bonnin D, Chabre Y, Masson V, Leriche JB, Tarascon JM: Effect of particle size on lithium intercalation into α -Fe₂O₃. *J Electrochem Soc* 2003, **150**:A133–A139.
65. Zhou W, Lin LJ, Wang WJ, Zhang LL, Wu QO, Li JH, Guo L: Hierarchical mesoporous hematite with “electron-transport channels” and its improved performances in photocatalysis and lithium ion batteries. *J Phys Chem C* 2011, **115**:7126–7133.
66. Cheng F, Huang KL, Liu SQ, Liu JL, Deng RJ: Surfactant carbonization to synthesize pseudocubic α -Fe₂O₃/c nanocomposite and its electrochemical performance in lithium-ion batteries. *Electrochim Acta* 2011, **56**:5593–5598.
67. Sun B, Horvat J, Kim HS, Kim WS, Ahn J, Wang GX: Synthesis of mesoporous α -Fe₂O₃ nanostructures for highly sensitive gas sensors and high capacity anode materials in lithium ion batteries. *J Phys Chem C* 2010, **114**:18753–18761.
68. Liu H, Wang GX, Park J, Wang J, Zhang C: Electrochemical performance of α -Fe₂O₃ nanorods as anode material for lithium-ion cells. *Electrochim Acta* 2009, **54**:1733–1736.
69. Reddy MV, Yu T, Sow CH, Shen ZX, Lim CT, Rao GVS, Chowdari BVR: α -Fe₂O₃ nanoflakes as an anode material for Li-ion batteries. *Adv Funct Mater* 2007, **17**:2792–2799.
70. Pan QT, Huang K, Ni SB, Yang F, Lin SM, He DY: Synthesis of α -Fe₂O₃ dendrites by a hydrothermal approach and their application in lithium-ion batteries. *J Phys D Appl Phys* 2009, **42**:015417.

doi:10.1186/1556-276X-8-2

Cite this article as: Zhu et al.: Hydrothermal evolution, optical and electrochemical properties of hierarchical porous hematite nanoarchitectures. *Nanoscale Research Letters* 2013 **8**:2.